An efficient 4-node facet shell element for the modified couple stress elasticity

Yan Shang[1, *], Huan-Pu Wu[1], Song Cen[2,3], Chen-Feng Li[4]

[1]*State Key Laboratory of Mechanics and Control of Mechanical Structures, College of Aerospace Engineering, Nanjing University of Aeronautics and Astronautics, Nanjing 210016, China*

[2]*Department of Engineering Mechanics, School of Aerospace Engineering, Tsinghua University, Beijing 100084, China*

[3]*School of Mechanics & Engineering, Liaoning Technical University, Fuxin 123000, China*

[4]*Zienkiewicz Centre for Computational Engineering and Energy Safety Research Institute, College of Engineering, Swansea University, Swansea SA1 8EN, UK*

*Corresponding author, E-mail: shangyan@nuaa.edu.cn

Abstract

This work proposes a simple but robust 4-node 24-DOF facet shell element for static analysis of small-scale thin shell structures. To accommodate the size effects, the modified couple stress theory is employed as the theoretical basis. The element is constructed via two main innovations. First, the trial functions that can a priori satisfy related governing differential equations are adopted as the basic functions for formulating the element interpolations. Second, the generalized conforming theory and the penalty function method are employed to meet the C^1 continuity requirement in weak sense for ensuring the computation convergence property. Several benchmarks of shells with different geometries are tested to assess the new facet shell element's capability. The numerical results reveal that the element can effectively simulate the size-dependent mechanical behaviors of small-scale thin shells, exhibiting satisfactory numerical accuracy and low susceptibility to mesh distortion. Moreover, as the shell element uses only six degrees of freedom per node, it can be incorporated into the commonly available finite element programs very readily.

Keywords: facet shell element; Kirchhoff-Love shell; modified couple stress theory; size effect; mesh distortion

1. Introduction

Because of efficient mechanical properties, the shell structures have extensive applications in small-scale devices, such as the components of the micro electromechanical system (MEMS) and the nano electromechanical system (NEMS) [1-3]. Numerous experimental evidences have indicated that the mechanical behaviors of small-scale structures are considerably size-dependent, and the classical continuum theory is insufficient for accurately describing the size effect. The atomic and molecular dynamic simulation methods are certainly conceptually valid for small length scales but almost always computationally intensive. On the other hand, the high-order continuum theories incorporating additional intrinsic material length scale parameters, such as the nonlocal theories [4-6], the strain gradient theories [7-9] and the couple stress theories [10-13], are capable of effectively simulating the size-dependent response of the small-scale structures. Among those high-order continuum theories, the modified couple stress theory proposed by Yang et al. [14] has become more and more popular due to its easy applicability and verifiability. In this development, the curvatures which are also considered in addition to the strains for contribution to the deformation energy are defined based on only the symmetric parts of rotation gradients. Consequently, just one intrinsic material length scale parameter is required to describe the size-dependence.

Based on the modified couple stress theory [14], a considerable amount of non-classical shell models has been successfully established in recent years. For instance, Zeighampour and Beni [15, 16] developed the thin cylindrical shell and conical shell models respectively for free vibration analysis of the single-walled carbon nanotube and nanocone; Jouneghani et al. [17] developed the first-order shear deformation shell model for orthotropic doubly curved micro shells; Ghayesh and Farokhi [18] studied the nonlinear mechanical behaviors of the doubly curved shallow micro shells; Hosseini-Hashemi et al. [19] proposed the size-dependent model for the closed micro/nano spherical shells; Ghadiri and Safarpour [20] performed the analysis of the cylindrical nano shell considering the magneto-electro-thermoelastic coupling effects; Wang et al. [21] investigated the vibration responses of the circular cylindrical polymeric shell reinforced by graphene platelet. Other contributions on micro/nano shell models based on the modified couple stress theory can be found in Beni et al. [22], Salehipour et al. [23], Wang et al. [24] and the references therein.

From the above literature review, one can clearly find that although the developments of size-

dependent shell models are quite successful, only limited problems with simple geometries and certain loading cases can be analytically solved because of the complexity of governing equations. Consequently, there is an urgent need to develop reliable numerical approaches with good accuracy and efficiency for practical engineering applications. As it is well known, the finite element method (FEM) is usually recognized as a very efficient tool to simulate the complicated behaviors of shells. The standard FE implementations of the size-dependent shell models naturally require more demanding displacement continuity. It is significant to notice that the high-order continuity requirement will bring great interpolation difficulties to element construction as well as make the element's performance more susceptible to mesh distortion. Over the past decades, tremendous efforts have been made to develop finite elements with concise formulation and satisfactory performance. But unfortunately, those existing works primarily focus on the membrane elements [25-31], solid elements [32-36] and plate bending elements [37-40]. The literatures regarding the shell elements, especially the ones which can be used for analysis of shells with complex geometries, are very limited [41].

The isogeometric analysis (IGA) proposed by Hughes et al. [42] which adopts the CAD basis functions as the shape functions is recently regards as an effective method to overcome the obstacle of high-order continuity [43, 44]. To name a few, Balobanov et al. [45] proposed an H^3-conforming IGA implementation for Kirchhoff-Love shells; Thai et al. [46] developed a nonlinear IGA thin shell element based on the modified couple stress theory; Schulte et al. [47] developed IGA shell elements for analysis of fiber reinforced composite materials. However, it's known that the IGA element ordinarily has a much larger support domain than the usual FEM, implying larger computational expense and more complicated formulation. Besides, the imposition of the boundary condition in the IGA still experiences some inadequacies.

To date, the FEM remains to be the most commonly used numerical tool in scientific and engineering computations. Thus, further efforts should be devoted to developing robust shell elements based on the high-order continuum theories. To this end, the objective of the current work is to propose a novel quadrilateral 4-node facet shell element in the framework of the modified couple stress theory for size-dependent static analysis of small-scale thin shells with complex geometries. Compared with other types of shell elements, the facet shell element can be constructed

and efficiently applied without complicated treatments in mathematical derivation [48]. Besides, it is more convenient in handling complex boundary conditions and analyzing folded plate structures. As mentioned above, the major difficulties encountered in developing the present facet shell element are the interpolation difficulty and mesh distortion sensitivity problems caused by the C^1 continuity requirement in the modified couple stress theory. To circumvent these obstacles, it is achieved with two main formulation innovations. First, the C^1 continuity requirement is satisfied in weak sense by using the generalized conforming theory [49] and the penalty function method without sacrificing the computation convergence property. Second, the trial functions that can a priori satisfy the related governing equations are introduced into the element construction to improve the element's performance in distorted meshes. Several well-established benchmark examples of shells with different geometric shapes are examined to validate the capability of the new facet shell element. It is observed that the element can effectively capture the size dependence of small-scale shell structures, exhibiting exceptional numerical accuracy and high tolerance to mesh distortion. Moreover, as the new element has only six degrees of freedom (DOF) per node, it can be incorporated into the commonly available finite element programs very readily.

2. Element Formulations

2.1. Overview of the modified couple stress elasticity

In the modified couple stress elasticity [14], the strains ε_{ij} and mechanical rotations ω_i are defined as the symmetric and skew-symmetric parts of the displacement gradients, respectively:

$$\varepsilon_{ij} = \frac{u_{i,j} + u_{j,i}}{2}, \quad \omega_i = \frac{1}{2} e_{ijk} u_{k,j} , \tag{1}$$

in which e_{ijk} is the permutation symbol. The curvatures χ_{ij} that are defined as the symmetric part of the rotation gradients are given by

$$\chi_{ij} = \frac{\omega_{i,j} + \omega_{j,i}}{2} . \tag{2}$$

For linear isotropic elastic materials, only one additional material length scale parameter l is required in the constitutive relationships to describe the size-dependent behaviors and thus, the stresses σ_{ij} and couple stresses m_{ij} can be calculated by

$$\sigma_{ij} = \lambda \varepsilon_{kk} \delta_{ij} + 2G \varepsilon_{ij}, \quad m_{ij} = 2Gl^2 \chi_{ij}. \tag{3}$$

in which λ and G are the two Lame's constants. Besides, the stresses and couple stresses should satisfy the following equilibrium equations:

$$\sigma_{ij,j} - \frac{1}{2} e_{ijk} m_{jm,mk} + f_i = 0, \tag{4}$$

in which f_i denotes the body force per unit volume.

The displacement boundary conditions in the modified couple stress theory [14] are given by

$$u_i = \bar{u}_i, \quad \omega_i - \left(n_j \omega_j\right) n_i = \bar{\omega}_i, \tag{5}$$

where $\bar{u}_i$ and $\bar{\omega}_i$ are the prescribed displacements and rotations along the boundary while n_j is the direction cosine of the outer normal direction. The traction boundary conditions are

$$n_j \sigma_{ij} - \frac{1}{2} e_{nmi} n_m m_{nj,j} - \bar{t}_i = 0, \quad n_j m_{ij} - \bar{c}_i = 0, \tag{6}$$

where $\bar{t}_i$ and $\bar{c}_i$ are the prescribed boundary stresses and couple stresses, respectively.

2.2. The basic equations for facet shell model

When using the facet shell elements to analyze the shell structure, the core idea is to approximate the shell's curved geometry by using a series of flat subdomains and each subdomain will be modeled by a facet shell element. Figure 1 briefly illustrates the schematic representation of a typical thin flat subdomain, in which the mid-surface is defined as the $\hat{x} - \hat{y}$ plane of the local Cartesian coordinate system, while $\hat{z}$ represents the thickness-direction $\left(-h/2 \le \hat{z} \le h/2\right)$ and h is the thickness. For brevity, the Voigt notation is used in the following sections and the style with cap over a character is used to denote the components defined in the local coordinate system.

By introducing the Kirchhoff-Love hypothesis and neglecting the coupling effects between the bending and membrane deformations at the subdomain level, the displacement vector $\hat{\mathbf{u}}$ with respect to the local Cartesian coordinate system $\left(\hat{x}, \hat{y}, \hat{z}\right)$ can be expressed by

$$\hat{\mathbf{u}} = \left\{ \begin{array}{c} \hat{u} \\ \hat{v} \\ \hat{w} \end{array} \right\} = \left\{ \begin{array}{c} \hat{u}_{\mathrm{m}}\left(\hat{x},\,\hat{y}\right) - \hat{z}\dfrac{\partial \hat{w}_{\mathrm{m}}\left(\hat{x},\,\hat{y}\right)}{\partial \hat{x}} \\[4mm] \hat{v}_{\mathrm{m}}\left(\hat{x},\,\hat{y}\right) - \hat{z}\dfrac{\partial \hat{w}_{\mathrm{m}}\left(\hat{x},\,\hat{y}\right)}{\partial \hat{y}} \\[4mm] \hat{w}_{\mathrm{m}}\left(\hat{x},\,\hat{y}\right) \end{array} \right\}, \tag{7}$$

in which $\hat{u}_{\mathrm{m}}, \hat{v}_{\mathrm{m}}$ and $\hat{w}_{\mathrm{m}}$ respectively are the three displacement components of the mid-surface. Therefore, the mid-surface can be employed as the reference plane for formulating the new facet shell element.

Next, by inserting Equation (7) into the kinematic equations of the modified couple stress theory [14], the non-zero strain vector $\hat{\boldsymbol{\varepsilon}}$ and physical rotation vector $\hat{\boldsymbol{\omega}}$ with respect to the local Cartesian coordinate system are obtained:

$$\hat{\boldsymbol{\varepsilon}} = \left\{ \begin{array}{c} \hat{\varepsilon}_{\hat{x}} \\ \hat{\varepsilon}_{\hat{y}} \\ 2\hat{\varepsilon}_{\hat{x}\hat{y}} \end{array} \right\} = \left\{ \begin{array}{c} \dfrac{\partial \hat{u}_{\mathrm{m}}}{\partial \hat{x}} - \hat{z}\dfrac{\partial^2 \hat{w}_{\mathrm{m}}}{\partial \hat{x}^2} \\[4mm] \dfrac{\partial \hat{v}_{\mathrm{m}}}{\partial \hat{y}} - \hat{z}\dfrac{\partial^2 \hat{w}_{\mathrm{m}}}{\partial \hat{y}^2} \\[4mm] \dfrac{\partial \hat{u}_{\mathrm{m}}}{\partial \hat{y}} + \dfrac{\partial \hat{v}_{\mathrm{m}}}{\partial \hat{x}} - 2\hat{z}\dfrac{\partial^2 \hat{w}_{\mathrm{m}}}{\partial \hat{x}\partial \hat{y}} \end{array} \right\}, \tag{8}$$

$$\hat{\boldsymbol{\omega}} = \left\{ \begin{array}{c} \hat{\omega}_{\hat{x}} \\ \hat{\omega}_{\hat{y}} \\ \hat{\omega}_{\hat{z}} \end{array} \right\} = \left\{ \begin{array}{c} \dfrac{\partial \hat{w}_{\mathrm{m}}}{\partial \hat{y}} \\[4mm] -\dfrac{\partial \hat{w}_{\mathrm{m}}}{\partial \hat{x}} \\[4mm] \dfrac{1}{2}\left(\dfrac{\partial \hat{v}_{\mathrm{m}}}{\partial \hat{x}} - \dfrac{\partial \hat{u}_{\mathrm{m}}}{\partial \hat{y}}\right) \end{array} \right\}. \tag{9}$$

Then, the non-zero curvature vector $\hat{\boldsymbol{\chi}}$ is further deduced:

$$\hat{\boldsymbol{\chi}} = \left\{ \begin{array}{c} \hat{\chi}_{\hat{x}} \\ \hat{\chi}_{\hat{y}} \\ 2\hat{\chi}_{\hat{x}\hat{y}} \\ 2\hat{\chi}_{\hat{x}\hat{z}} \\ 2\hat{\chi}_{\hat{y}\hat{z}} \end{array} \right\} = \left\{ \begin{array}{c} \dfrac{\partial \hat{\omega}_{\hat{x}}}{\partial \hat{x}} \\[4mm] \dfrac{\partial \hat{\omega}_{\hat{y}}}{\partial \hat{y}} \\[4mm] \dfrac{\partial \hat{\omega}_{\hat{x}}}{\partial \hat{y}} + \dfrac{\partial \hat{\omega}_{\hat{y}}}{\partial \hat{x}} \\[4mm] \dfrac{\partial \hat{\omega}_{\hat{z}}}{\partial \hat{x}} \\[4mm] \dfrac{\partial \hat{\omega}_{\hat{z}}}{\partial \hat{y}} \end{array} \right\}. \tag{10}$$

As suggested by [50], in the present model, the stress vector $\hat{\boldsymbol{\sigma}}$ and couple stress vector $\hat{\mathbf{m}}$

which respectively are the work conjugate pairs of the above strain $\hat{\boldsymbol{\varepsilon}}$ and curvature $\hat{\boldsymbol{\chi}}$ are derived using the reduced constitutive relationship of the plane stress state instead of the original three-dimensional ones:

$$\hat{\boldsymbol{\sigma}} = \begin{Bmatrix} \hat{\sigma}_{\hat{x}} \\ \hat{\sigma}_{\hat{y}} \\ \hat{\sigma}_{\hat{x}\hat{y}} \end{Bmatrix} = \mathbf{D}_\varepsilon \hat{\boldsymbol{\varepsilon}}, \quad \mathbf{D}_\varepsilon = \begin{bmatrix} E/(1-v^2) & Ev/(1-v^2) & 0 \\ Ev/(1-v^2) & E/(1-v^2) & 0 \\ 0 & 0 & G \end{bmatrix}, \tag{11}$$

$$\hat{\mathbf{m}} = \begin{Bmatrix} \hat{m}_{\hat{x}} \\ \hat{m}_{\hat{y}} \\ \hat{m}_{\hat{x}\hat{y}} \\ \hat{m}_{\hat{x}\hat{z}} \\ \hat{m}_{\hat{y}\hat{z}} \end{Bmatrix} = \mathbf{D}_\chi \hat{\boldsymbol{\chi}}, \quad \mathbf{D}_\chi = \begin{bmatrix} 2Gl^2 & & & & \\ & 2Gl^2 & & & \\ & & Gl^2 & & \\ & & & Gl^2 & \\ & & & & Gl^2 \end{bmatrix}, \tag{12}$$

in which E is Young's modulus, v is Poisson's ratio and $G = E/2(1+v)$.

2.3. The formulations of the new facet shell element

Let us consider a quadrilateral 4-node 24-DOF facet shell element as shown in Figure 2, in which 1~4 denote the element nodes whilst 5~8 are the mid-side points of the element's four edges. The element nodal DOF vector $\mathbf{a}^e$ with respect to the global Cartesian coordinate system (x, y, z) is

$$\mathbf{a}^e = \begin{bmatrix} \mathbf{a}_1^e & \mathbf{a}_2^e & \mathbf{a}_3^e & \mathbf{a}_4^e \end{bmatrix}^{\mathrm{T}}, \tag{13}$$

with

$$\mathbf{a}_i^e = [u_i \quad v_i \quad w_i \quad \theta_{xi} \quad \theta_{yi} \quad \theta_{zi}], \quad (i = 1 \sim 4). \tag{14}$$

2.3.1 The relationship between the global and local coordinate systems

Regarding that the four mid-side points 5~8 are always coplanar even though the geometry of the shell element is warped, the local Cartesian coordinate system $(\hat{x}, \hat{y}, \hat{z})$ which is attached to the facet shell element is established in accordance with the position of the planar face 5678. The intersection point C is set as the origin of the local Cartesian coordinate system. The base vectors of the $\hat{x}$- and $\hat{z}$- axes are respectively determined by

7

$$\mathbf{e}_{\hat{x}} = \frac{\mathbf{V}_1}{\|\mathbf{V}_1\|_2}, \quad \mathbf{V}_1 = \begin{Bmatrix} x_7 - x_5 \\ y_7 - y_5 \\ z_7 - z_5 \end{Bmatrix}, \tag{15}$$

and

$$\mathbf{e}_{\hat{z}} = \frac{\mathbf{V}_3}{\|\mathbf{V}_3\|_2}, \quad \mathbf{V}_3 = \mathbf{V}_1 \times \mathbf{V}_2, \quad \mathbf{V}_2 = \begin{Bmatrix} x_8 - x_6 \\ y_8 - y_6 \\ z_8 - z_6 \end{Bmatrix}, \tag{16}$$

in which (x_i, y_i, z_i), $(i = 5 \sim 8)$ are the global Cartesian coordinates of the mid-side points 5~8; the symbol $\times$ denotes the cross product of vectors and $\|.\|_2$ is to calculate the length of a vector. Besides, the base vector of the $\hat{y}$- axis is given by

$$\mathbf{e}_{\hat{y}} = \frac{\mathbf{V}_3 \times \mathbf{V}_1}{\|\mathbf{V}_3 \times \mathbf{V}_1\|_2}. \tag{17}$$

Making use of the foregoing definitions, the transformation relationship between the local Cartesian coordinates and the global Cartesian coordinates is obtained as follows:

$$\begin{Bmatrix} \hat{x} \\ \hat{y} \\ \hat{z} \end{Bmatrix} = \boldsymbol{\lambda} \begin{Bmatrix} x - x_C \\ y - y_C \\ z - z_C \end{Bmatrix}, \quad \boldsymbol{\lambda} = \begin{bmatrix} \mathbf{e}_{\hat{x}} & \mathbf{e}_{\hat{y}} & \mathbf{e}_{\hat{z}} \end{bmatrix}^{\mathrm{T}}, \tag{18}$$

where (x_C, y_C, z_C) are the global Cartesian coordinates of the intersection point C. Accordingly, the element nodal DOF vector $\hat{\mathbf{a}}^e$ with respect to the above local Cartesian coordinate system $(\hat{x}, \hat{y}, \hat{z})$ is

$$\hat{\mathbf{a}}^e = \begin{bmatrix} \hat{\mathbf{a}}_1^e & \hat{\mathbf{a}}_2^e & \hat{\mathbf{a}}_3^e & \hat{\mathbf{a}}_4^e \end{bmatrix}^{\mathrm{T}}, \tag{19}$$

with

$$\hat{\mathbf{a}}_i^e = [\hat{u}_i \quad \hat{v}_i \quad \hat{w}_i \quad \hat{\theta}_{\hat{x}i} \quad \hat{\theta}_{\hat{y}i} \quad \hat{\theta}_{\hat{z}i}], \quad (i = 1 \sim 4). \tag{20}$$

The relationship between $\hat{\mathbf{a}}^e$ and $\mathbf{a}^e$ is given by

$$\hat{\mathbf{a}}^e = \mathbf{T}\mathbf{a}^e, \tag{21}$$

where

$$\mathbf{T} = \begin{bmatrix} \mathbf{t} & & & \\ & \mathbf{t} & & \\ & & \mathbf{t} & \\ & & & \mathbf{t} \end{bmatrix}, \quad \mathbf{t} = \begin{bmatrix} \boldsymbol{\lambda} & \\ & \boldsymbol{\lambda} \end{bmatrix}, \tag{22}$$

in which the matrix $\boldsymbol{\lambda}$ is given by Equation (18).

As preceding discussed, the coupling effects of the bending and membrane deformations are neglected at the element level. Therefore, when designing the element interpolations in the local Cartesian coordinate system, the out-of-plane displacement $\hat{w}_{\mathrm{m}}(\hat{x}, \hat{y})$ which corresponds to the bending behaviors and the other two components $\hat{u}_m(\hat{x}, \hat{y})$ and $\hat{v}_m(\hat{x}, \hat{y})$ which correspond to the membrane deformations can be constructed independently. Accordingly, the element nodal DOF vector $\hat{\mathbf{a}}^e$ given in Equation (19) can be divided into the out-of-plane group $\hat{\mathbf{a}}_b^e$ and the in-plane group $\hat{\mathbf{a}}_m^e$, which respectively are for describing the bending and membrane deformations:

$$\hat{\mathbf{a}}_b^e = \begin{bmatrix} \hat{\mathbf{a}}_{b1}^e & \hat{\mathbf{a}}_{b2}^e & \hat{\mathbf{a}}_{b3}^e & \hat{\mathbf{a}}_{b4}^e \end{bmatrix}^{\mathrm{T}}, \quad \hat{\mathbf{a}}_{bi}^e = [\hat{w}_i \quad \hat{\theta}_{\hat{x}i} \quad \hat{\theta}_{\hat{y}i}], \ (i = 1 \sim 4), \tag{23}$$

$$\hat{\mathbf{a}}_m^e = \begin{bmatrix} \hat{\mathbf{a}}_{m1}^e & \hat{\mathbf{a}}_{m2}^e & \hat{\mathbf{a}}_{m3}^e & \hat{\mathbf{a}}_{m4}^e \end{bmatrix}^{\mathrm{T}}, \quad \hat{\mathbf{a}}_{mi}^e = [\hat{u}_i \quad \hat{v}_i \quad \hat{\theta}_{\hat{z}i}], \ (i = 1 \sim 4). \tag{24}$$

2.3.2 The interpolations related to the bending deformations

Since the out-of-plane displacement of the mid-surface $\hat{w}_{\mathrm{m}}(\hat{x}, \hat{y})$ is related only to the bending deformations, it can be initially assumed as the linear combination of the Trefftz functions of the micro thin plate bending problem [39] in the context of the modified couple stress theory:

$$\hat{w}_{\mathrm{m}}(\hat{x}, \hat{y}) = \mathbf{W}\boldsymbol{\alpha}, \tag{25}$$

in which

$$\mathbf{W} = \begin{bmatrix} 1 & \hat{x} & \hat{y} & \hat{x}^2 & \hat{x}\hat{y} & \hat{y}^2 & \hat{x}^3 & \hat{x}^2\hat{y} & \hat{x}\hat{y}^2 & \hat{y}^3 & \hat{x}^3\hat{y} & \hat{x}\hat{y}^3 & \hat{x}^4 - \hat{y}^4 & 6\hat{x}^2\hat{y}^2 - \hat{x}^4 - \hat{y}^4 \end{bmatrix}, \tag{26}$$

$$\boldsymbol{\alpha} = \begin{bmatrix} \alpha_1 & \alpha_2 & \dots & \alpha_{14} \end{bmatrix}^{\mathrm{T}}. \tag{27}$$

It's noted that the above assumed out-of-plane displacement field $\hat{w}_{\mathrm{m}}$ can satisfy the homogeneous governing differential equations of the concerned bending problem of the micro thin plate. For more details, one can kindly refer to the reference [39].

Next, the coming fourteen compatibility conditions which are chosen based on the generalized conforming theory [49, 51] are employed to obtain the relation between the introduced coefficient $\boldsymbol{\alpha}$ and the element nodal DOFs:

(I) at the four nodes 1~4,

$$\hat{w}_{\mathrm{m}}\left(\hat{x}_i, \hat{y}_i\right) = \hat{w}_i, \quad \left(i = 1 \sim 4\right), \tag{28}$$

in which the left-hand side of the equation is the deflection calculated by substituting the local Cartesian coordinates into Equation (25), whilst the right-hand item is the corresponding nodal transverse displacement DOF listed in Equation (23);

(II) at the eight points as illustrated in Figure 3,

$$\frac{\partial \hat{w}_{\mathrm{m}}\left(\hat{x}_k, \hat{y}_k\right)}{\partial n} = \bar{\psi}_{nk}, \quad \left(k = A_1, B_1, A_2, B_2, A_3, B_3, A_4, B_4\right), \tag{29}$$

in which n is the outer normal direction of the element's edge and for the edge ij; the right-hand item is calculated by substituting the Gaussian parametric coordinate ξ of the point k into the following function:

$$\bar{\psi}_{nij} = \left(\frac{1-\xi}{2}\right)\left(-\hat{s}_{ij}\hat{\theta}_{\hat{y}i} + \hat{c}_{ij}\hat{\theta}_{\hat{x}i}\right) + \frac{1+\xi}{2}\left(-\hat{s}_{ij}\hat{\theta}_{\hat{y}j} + \hat{c}_{ij}\hat{\theta}_{\hat{x}j}\right), \quad \left(ij = 12, 23, 34, 41\right), \tag{30}$$

where $\left(\hat{s}_{ij}, \hat{c}_{ij}\right)$ are the direction cosines of the outer normal direction n with respect to the local Cartesian coordinate system; $\hat{\theta}_{\hat{x}i}$, $\hat{\theta}_{\hat{y}i}$, $\hat{\theta}_{\hat{x}j}$ and $\hat{\theta}_{\hat{y}j}$ are the nodal rotation DOFs listed in Equation (23);

(III) at the four mid-side points 5~8,

$$\hat{w}_{\mathrm{m}}(\hat{x}_5, \hat{y}_5) + \hat{w}_{\mathrm{m}}(\hat{x}_7, \hat{y}_7) = \hat{w}_5 + \hat{w}_7, \tag{31}$$

$$\hat{w}_{\mathrm{m}}(\hat{x}_6, \hat{y}_6) + \hat{w}_{\mathrm{m}}(\hat{x}_8, \hat{y}_8) = \hat{w}_6 + \hat{w}_8, \tag{32}$$

in which the left-hand items are obtained in accordance with Equation (25) and the right-hand items are calculated by

$$\hat{w}_{i+4} = \frac{1}{2}\hat{w}_i + \frac{1}{2}\hat{w}_j + \frac{l_{ij}}{8}\left(\hat{s}_{ij}\hat{\theta}_{\hat{y}i} + \hat{c}_{ij}\hat{\theta}_{\hat{x}i}\right) - \frac{l_{ij}}{8}\left(\hat{s}_{ij}\hat{\theta}_{\hat{y}j} + \hat{c}_{ij}\hat{\theta}_{\hat{x}j}\right), \quad \left(ij = 12, 23, 34, 41\right), \tag{33}$$

where l_{ij} is the length of the element edge ij.

In our previous works [39, 52], it has been proved that the above set of fourteen conditions can effectively meet the C^1 compatibility requirement of the Kirchhoff thin plate in weak sense. In

general, the requirement is satisfied more strictly as the mesh being gradually refined. For more details of the generalized conforming theory, one can kindly refer to [51, 52].

From these conditions, the coefficient vector $\boldsymbol{\alpha}$ can be finally expressed in terms of the vector $\hat{\mathbf{a}}_b^e$ in Equation (23):

$$\boldsymbol{\alpha} = \mathbf{Z}\hat{\mathbf{a}}_b^e, \tag{34}$$

and therefore, the transverse displacement of the mid-surface $\hat{w}_m(\hat{x}, \hat{y})$ is rewritten as

$$\hat{w}_m(\hat{x}, \hat{y}) = \mathbf{WZ}\hat{\mathbf{a}}_b^e. \tag{35}$$

By inserting Equation (35) back into Equation (9), the deduced physical rotations are obtained:

$$\left\{ \begin{matrix} \hat{\omega}_{\hat{x}} \\ \hat{\omega}_{\hat{y}} \end{matrix} \right\} = \boldsymbol{\Psi}\mathbf{Z}\hat{\mathbf{a}}_b^e, \tag{36}$$

with

$$\boldsymbol{\Psi} = \begin{bmatrix} 0 & 0 & 1 & 0 & \hat{x} & 2\hat{y} & 0 & \hat{x}^2 & 2\hat{x}\hat{y} & 3\hat{y}^2 & \hat{x}^3 & 3\hat{x}\hat{y}^2 & -4\hat{y}^3 & 12\hat{x}^2\hat{y}-4\hat{y}^3 \\ 0 & -1 & 0 & -2\hat{x} & -\hat{y} & 0 & -3\hat{x}^2 & -2\hat{x}\hat{y} & -\hat{y}^2 & 0 & -3\hat{x}^2\hat{y} & -\hat{y}^3 & -4\hat{x}^3 & 4\hat{x}^3-12\hat{x}\hat{y}^2 \end{bmatrix}. \tag{37}$$

Next, substitutions of Equations (35) and (36) respectively into Equations (8) and (10) further yield

$$\left\{ \begin{matrix} -\hat{z}\dfrac{\partial^2 \hat{w}_m}{\partial \hat{x}^2} \\[2mm] -\hat{z}\dfrac{\partial^2 \hat{w}_m}{\partial \hat{y}^2} \\[2mm] -2\hat{z}\dfrac{\partial^2 \hat{w}_m}{\partial \hat{x}\partial \hat{y}} \end{matrix} \right\} = \mathbf{QZ}\hat{\mathbf{a}}_b^e, \tag{38}$$

$$\left\{ \begin{matrix} \dfrac{\partial \hat{\omega}_{\hat{x}}}{\partial \hat{x}} \\[2mm] \dfrac{\partial \hat{\omega}_{\hat{y}}}{\partial \hat{y}} \\[2mm] \dfrac{\partial \hat{\omega}_{\hat{x}}}{\partial \hat{y}} + \dfrac{\partial \hat{\omega}_{\hat{y}}}{\partial \hat{x}} \end{matrix} \right\} = \boldsymbol{\Theta}\boldsymbol{\alpha} = \boldsymbol{\Theta}\mathbf{Z}\hat{\mathbf{a}}_b^e, \tag{39}$$

in which

$$\mathbf{Q} = -\hat{z}\begin{bmatrix} 0 & 0 & 0 & 2 & 0 & 0 & 6\hat{x} & 2\hat{y} & 0 & 0 & 6\hat{x}\hat{y} & 0 & 12\hat{x}^2 & 12\hat{y}^2-12\hat{x}^2 \\ 0 & 0 & 0 & 0 & 0 & 2 & 0 & 0 & 2\hat{x} & 6\hat{y} & 0 & 6\hat{x}\hat{y} & -12\hat{y}^2 & 12\hat{x}^2-12\hat{y}^2 \\ 0 & 0 & 0 & 0 & 2 & 0 & 0 & 4\hat{x} & 4\hat{y} & 0 & 6\hat{x}^2 & 6\hat{y}^2 & 0 & 48\hat{x}\hat{y} \end{bmatrix}, \tag{40}$$

11

$$
\Theta = \begin{bmatrix} 0 & 0 & 0 & 0 & 1 & 0 & 0 & 2\hat{x} & 2\hat{y} & 0 & 3\hat{x}^2 & 3\hat{y}^2 & 0 & 24\hat{x}\hat{y} \\ 0 & 0 & 0 & 0 & -1 & 0 & 0 & -2\hat{x} & -2\hat{y} & 0 & -3\hat{x}^2 & -3\hat{y}^2 & 0 & -24\hat{x}\hat{y} \\ 0 & 0 & 0 & -2 & 0 & 2 & -6\hat{x} & -2\hat{y} & 2\hat{x} & 6\hat{y} & -6\hat{x}\hat{y} & 6\hat{x}\hat{y} & -12\hat{y}^2 - 12\hat{x}^2 & 24\hat{x}^2 - 24\hat{y}^2 \end{bmatrix}.
$$

(41)

2.3.3 The interpolations related to the membrane deformations

When formulating the two in-plane displacement components of the mid-surface $\hat{u}_{\mathrm{m}}(\hat{x}, \hat{y})$ and $\hat{v}_m(\hat{x}, \hat{y})$ that are only related to the membrane deformations, the C^1 interelement compatibility requirements will be satisfied in weak form by using the penalty function method, enabling the usage of C^0 continuous shape functions as the element interpolations. Firstly, these two displacements are interpolated by the element's in-plane DOF vector $\hat{\mathbf{a}}_m^e$ as follows:

$$
\begin{Bmatrix} \hat{u}_{\mathrm{m}} \\ \hat{v}_{\mathrm{m}} \end{Bmatrix} = \mathbf{N}_{\mathrm{m}} \hat{\mathbf{a}}_m^e, \quad \mathbf{N}_{\mathrm{m}} = \begin{bmatrix} \mathbf{N}_1 & \mathbf{N}_2 & \mathbf{N}_3 & \mathbf{N}_4 \end{bmatrix},
$$

(42)

with

$$
\mathbf{N}_i = \begin{bmatrix} N_i & 0 & -\dfrac{1}{2} N_i (\hat{y} - \hat{y}_i) \\ 0 & N_i & \dfrac{1}{2} N_i (\hat{x} - \hat{x}_i) \end{bmatrix}, \quad i = 1 \sim 4,
$$

(43)

in which N_i is the standard isoparametric shape function:

$$
\begin{cases} N_1 = \dfrac{1}{4}(1-\xi)(1-\eta), & N_2 = \dfrac{1}{4}(1+\xi)(1-\eta) \\ N_3 = \dfrac{1}{4}(1+\xi)(1+\eta), & N_4 = \dfrac{1}{4}(1-\xi)(1+\eta) \end{cases}.
$$

(44)

Note that the above displacement interpolation will coincide with the conventional Allman's interpolation [53] along the element boundaries but has a more concise expression. Accordingly, substitution of Equation (42) into Equation (8) yields

$$
\begin{Bmatrix} \dfrac{\partial \hat{u}_{\mathrm{m}}}{\partial \hat{x}} \\ \dfrac{\partial \hat{v}_{\mathrm{m}}}{\partial \hat{y}} \\ \dfrac{\partial \hat{u}_{\mathrm{m}}}{\partial \hat{y}} + \dfrac{\partial \hat{u}_{\mathrm{m}}}{\partial \hat{x}} \end{Bmatrix} = \mathbf{\Gamma} \hat{\mathbf{a}}_m^e, \quad \mathbf{\Gamma} = \begin{bmatrix} \mathbf{\Gamma}_1 & \mathbf{\Gamma}_2 & \mathbf{\Gamma}_3 & \mathbf{\Gamma}_4 \end{bmatrix},
$$

(45)

with

$$\mathbf{\Gamma}_i = \begin{bmatrix} N_{i,\hat{x}} & 0 & -\dfrac{1}{2}N_{i,\hat{x}}\left(\hat{y}-\hat{y}_i\right) \\[2mm] 0 & N_{i,\hat{y}} & \dfrac{1}{2}N_{i,\hat{y}}\left(\hat{x}-\hat{x}_i\right) \\[2mm] N_{i,\hat{y}} & N_{i,\hat{x}} & \dfrac{1}{2}N_{i,\hat{x}}\left(\hat{x}-\hat{x}_i\right)-\dfrac{1}{2}N_{i,\hat{x}}\left(\hat{y}-\hat{y}_i\right) \end{bmatrix}, \quad i=1\sim4. \tag{46}$$

Besides, instead of being directly derived from the displacements using the kinematic equation as shown in Equation (9), the physical rotation $\hat{\omega}_{\hat{z}}$ is approximated by an independently assumed rotation field:

$$\hat{\omega}_{\hat{z}} = \mathbf{N}^{\theta}\hat{\mathbf{a}}_m^e, \tag{47}$$

with

$$\mathbf{N}^{\theta} = \begin{bmatrix} 0 & 0 & N_1 & 0 & 0 & N_2 & 0 & 0 & N_3 & 0 & 0 & N_4 \end{bmatrix}. \tag{48}$$

The penalty function method is employed to constrain the difference $\Lambda \to 0$:

$$\Lambda = \frac{1}{2}\left(\frac{\partial \hat{v}_{\mathrm{m}}}{\partial \hat{x}} - \frac{\partial \hat{u}_{\mathrm{m}}}{\partial \hat{y}}\right) - \hat{\omega}_{\hat{z}} = \mathbf{N}_m^{\Lambda}\hat{\mathbf{a}}_m^e, \quad \mathbf{N}_m^{\Lambda} = \begin{bmatrix} \mathbf{N}_{m1}^{\Lambda} & \mathbf{N}_{m2}^{\Lambda} & \mathbf{N}_{m3}^{\Lambda} & \mathbf{N}_{m4}^{\Lambda} \end{bmatrix}, \tag{49}$$

where

$$\mathbf{N}_{mi}^{\Lambda} = \frac{1}{2}\left[-N_{i,\hat{y}} \quad N_{i,\hat{x}} \quad \frac{1}{2}N_{i,\hat{x}}\left(\hat{x}-\hat{x}_i\right)+\frac{1}{2}N_{i,\hat{y}}\left(\hat{y}-\hat{y}_i\right)-N_i \right], \quad i=1\sim4. \tag{50}$$

Afterwards, by substituting Equation (47) into Equation (10), we can get

$$\begin{Bmatrix} \dfrac{\partial \hat{\omega}_{\hat{z}}}{\partial \hat{x}} \\[2mm] \dfrac{\partial \hat{\omega}_{\hat{z}}}{\partial \hat{y}} \end{Bmatrix} = \mathbf{P}\hat{\mathbf{a}}_m^e, \tag{51}$$

with

$$\mathbf{P} = \begin{bmatrix} 0 & 0 & N_{1,\hat{x}} & 0 & 0 & N_{2,\hat{x}} & 0 & 0 & N_{3,\hat{x}} & 0 & 0 & N_{4,\hat{x}} \\ 0 & 0 & N_{1,\hat{y}} & 0 & 0 & N_{2,\hat{y}} & 0 & 0 & N_{3,\hat{y}} & 0 & 0 & N_{4,\hat{y}} \end{bmatrix}. \tag{52}$$

It's worth pointing out that the strain interpolation given by Equation (45) still delivers unsatisfactory performances in distorted meshes even though the strains have been enriched by the nodal rotation DOFs through the linked interpolation technique [54]. For purpose of effectively improving the element's performance in distorted meshes, inspired by the hybrid stress function method [55] which is developed for the classical elasticity, the following substitute strain field are

introduced:

$$\left\{\begin{array}{c} \dfrac{\partial \hat{u}_{\mathrm{m}}}{\partial \hat{x}} \\[6pt] \dfrac{\partial \hat{v}_{\mathrm{m}}}{\partial \hat{y}} \\[6pt] \dfrac{\partial \hat{u}_{\mathrm{m}}}{\partial \hat{y}} + \dfrac{\partial \hat{v}_{\mathrm{m}}}{\partial \hat{x}} \end{array}\right\}_{\text{substitute}} = \mathbf{D}_{\varepsilon}^{-1}\mathbf{H}\boldsymbol{\beta}, \tag{53}$$

with

$$\mathbf{H} = \begin{bmatrix} 0 & 0 & 2 & 0 & 0 & 2\hat{x} & 6\hat{y} \\ 2 & 0 & 0 & 6\hat{x} & 2\hat{y} & 0 & 0 \\ 0 & -1 & 0 & 0 & -2\hat{x} & -2\hat{y} & 0 \end{bmatrix}, \tag{54}$$

$$\boldsymbol{\beta} = \begin{bmatrix} \beta_1 & \beta_2 & \cdots & \beta_7 \end{bmatrix}^{\mathrm{T}}, \tag{55}$$

where $\mathbf{D}_{\varepsilon}$ is given by Equation (11) and $\mathbf{H}$ consists of the Airy stress trial functions that can a priori satisfy the governing equations of the plane stress problem.

The weighted residual method is employed to establish the relationship between this substitute strain and the original one given in Equation (45):

$$\int_{\Omega} \mathbf{H}^{\mathrm{T}}\left(\boldsymbol{\Gamma}\hat{\mathbf{a}}_{m}^{e} - \mathbf{D}_{\varepsilon}^{-1}\mathbf{H}\boldsymbol{\beta}\right)h\mathrm{d}\Omega = \mathbf{0}, \tag{56}$$

in which Ω represents the domain of the element's reference plane. From Equation (56), we can get

$$\boldsymbol{\beta} = \mathbf{M}^{-1}\mathbf{V}\hat{\mathbf{a}}_{m}^{e}, \tag{57}$$

with

$$\mathbf{M} = \int_{\Omega} \mathbf{H}^{\mathrm{T}}\mathbf{D}_{\varepsilon}^{-1}\mathbf{H}h\mathrm{d}\Omega, \tag{58}$$

$$\mathbf{V} = \int_{\Omega} \mathbf{H}^{\mathrm{T}}\boldsymbol{\Gamma}h\mathrm{d}\Omega. \tag{59}$$

Next, by substituting Equation (57) back into Equation (53), we can obtain the final expression of the substitute strain:

14

$$\underset{\text{substitute}}{\left\{ \begin{array}{c} \dfrac{\partial \hat{u}_{\mathrm{m}}}{\partial \hat{x}} \\[2mm] \dfrac{\partial \hat{v}_{\mathrm{m}}}{\partial \hat{y}} \\[2mm] \dfrac{\partial \hat{u}_{\mathrm{m}}}{\partial \hat{y}} + \dfrac{\partial \hat{v}_{\mathrm{m}}}{\partial \hat{x}} \end{array} \right\}} = \mathbf{D}_{\varepsilon}^{-1}\mathbf{H}\mathbf{M}^{-1}\mathbf{V}\hat{\mathbf{a}}_{m}^{e} . \tag{60}$$

2.3.3 The element stiffness matrix

By substituting Equations (38) and (60) back into Equation (8) and assembling their components in accordance with the DOFs' sequence in Equation (19), the final integrated form of the strain interpolation which is expressed in terms of $\hat{\mathbf{a}}^{e}$ is delivered:

$$\hat{\boldsymbol{\varepsilon}} = \left\{ \begin{array}{c} \hat{\varepsilon}_{\hat{x}} \\ \hat{\varepsilon}_{\hat{y}} \\ 2\hat{\varepsilon}_{\hat{x}\hat{y}} \end{array} \right\} = \mathbf{B}_{\varepsilon}\hat{\mathbf{a}}^{e} . \tag{61}$$

Simultaneously, substations of Equations (39) and (51) back into Equation (10) also yield the final expression of the curvature interpolation:

$$\hat{\boldsymbol{\chi}} = \left\{ \begin{array}{c} \hat{\chi}_{\hat{x}} \\ \hat{\chi}_{\hat{y}} \\ 2\hat{\chi}_{\hat{x}\hat{y}} \\ 2\hat{\chi}_{\hat{x}\hat{z}} \\ 2\hat{\chi}_{\hat{y}\hat{z}} \end{array} \right\} = \mathbf{B}_{\chi}\hat{\mathbf{a}}^{e} . \tag{62}$$

Now that the element stain and curvature interpolations have been determined, the element stiffness matrix with respect to the local Cartesian coordinate system can be derived by simply applying the principle of minimum potential energy:

$$\mathbf{K} = \int_{-\frac{h}{2}}^{\frac{h}{2}} \int_{\Omega} \left(\mathbf{B}_{\varepsilon}^{\mathrm{T}} \mathbf{D}_{\varepsilon} \mathbf{B}_{\varepsilon} + \mathbf{B}_{\chi}^{\mathrm{T}} \mathbf{D}_{\chi} \mathbf{B}_{\chi} \right) \mathrm{d}\Omega \mathrm{d}z + k \int_{-\frac{h}{2}}^{\frac{h}{2}} \int_{\Omega} \mathbf{N}^{\Lambda \mathrm{T}} \mathbf{N}^{\Lambda} \, \mathrm{d}\Omega \mathrm{d}z , \tag{63}$$

in which the last item is the penalty stiffness matrix because of the usage of the penalty function method to impose the constraint $\Lambda \rightarrow 0$ shown in Equation (49); $\mathbf{N}^{\Lambda}$ is derived from Equation (50) and has the expression:

$$\mathbf{N}^{\Lambda} = \begin{bmatrix} \mathbf{N}_{1}^{\Lambda} & \mathbf{N}_{2}^{\Lambda} & \mathbf{N}_{3}^{\Lambda} & \mathbf{N}_{4}^{\Lambda} \end{bmatrix} , \tag{64}$$

$$\mathbf{N}_{i}^{\Lambda} = \frac{1}{2}\begin{bmatrix} -N_{i,\hat{y}} & N_{i,\hat{x}} & 0 & 0 & 0 & \frac{1}{2}N_{i,\hat{x}}\left(\hat{x}-\hat{x}_{i}\right)+\frac{1}{2}N_{i,\hat{y}}\left(\hat{y}-\hat{y}_{i}\right)-N_{i} \end{bmatrix}, \quad i = 1 \sim 4 ; \tag{65}$$

15

k is the penalty parameter and in general, the constraint is satisfied more strictly as the penalty parameter increases. The numerical results of the parametric studies reveal that $k/G = 10^4$ is an appropriate value that can enforce the constraint at an acceptable level and doesn't make the stiffness matrix ill conditioned. The penalty stiffness part is integrated by using the one-point quadrature strategy for eliminating the possible locking problem [56-59] while the other items are calculated using the full quadrature scheme.

As previously discussed, in general, the geometry of a quadrilateral 4-node shell element is warped. The element stiffness matrix obtained by following the above process is formulated actually in accordance with the projected flat plane $1'2'3'4'$ instead of the real domain 1234, as shown in Figure 4. Therefore, in order to take the influence of the geometry warpage into consideration, the rigid link correction strategy [60] is employed here for modifying the element stiffness matrix:

$$\mathbf{K}_{\text{local}} = \mathbf{X}\mathbf{K}\mathbf{X}^{\text{T}}, \tag{66}$$

with

$$\mathbf{X} = \begin{bmatrix} \mathbf{X}_1 & & & \\ & \mathbf{X}_2 & & \\ & & \mathbf{X}_3 & \\ & & & \mathbf{X}_4 \end{bmatrix}, \quad \mathbf{X}_i = \begin{bmatrix} 1 & & & & & \\ 0 & 1 & & & & \\ 0 & 0 & 1 & & & \\ 0 & \hat{z}_i & 0 & 1 & & \\ -\hat{z}_i & 0 & 0 & 0 & 1 & \\ 0 & 0 & 0 & 0 & 0 & 1 \end{bmatrix}, \tag{67}$$

in which $\hat{z}_i$ is the local Cartesian coordinate of the node i.

Finally, the element stiffness matrix with respect to the global Cartesian coordinate system can be obtained by

$$\mathbf{K}_{\text{global}} = \mathbf{T}^{\text{T}}\mathbf{K}_{\text{local}}\mathbf{T}, \tag{68}$$

in which the matrix $\mathbf{T}$ has been given in Equation (21).

It is worth noting that the new facet shell element still uses the same nodal DOFs with the conventional ones which are based on the classical continuum theory. Thus, it can be directly integrated into the existing finite element programs without special treatments. For instance, the new element can be incorporated into the commonly used FE software Abaqus through the user element subroutine [61] very readily.

3. Numerical Examples

For purpose of validating the capability of the new quadrilateral 4-node facet shell element in analyzing the size-dependent mechanical responses of small-scale shells with different complex geometric shapes, several classical benchmark examples are extended to the modified couple stress elasticity. Since the closed-form solutions of these problems are unavailable in the open literature, the numerical overkill solutions obtained by using the three-dimensional (3D) hexahedral solid element proposed in [35] are employed as the reference values.

3.1. The patch test

Figure 5 illustrates the model and typical meshes used for the patch test for assessing the convergence property of the new element with the flat plate geometry. The displacements and rotations calculated at the boundary nodes in accordance with the given functions are imposed to the patch as the prescribed boundary conditions, whilst the values at the inner nodes are monitored. First, the following functions related to the bending deformation in constant rotation gradient state are considered:

$$w = x^2 + y^2 + xy, \quad \theta_x = 2y + x, \quad \theta_y = -2x - y, \tag{69}$$

and it is shown that the exact results can always be delivered by the new element. Second, the functions that correspond to the membrane deformation in constant rotation gradient state [62] is considered:

$$u = x^2 - (6 - 8v)xy + y^2, \quad v = x^2 - (6 - 8v)xy + y^2, \quad \theta_z = 4(1 - v)(x - y). \tag{70}$$

The numerical results reveal that the element can strictly pass the test when the regular mesh is used whilst some errors are experienced in distorted meshes due to that the C^1 compatibility requirements for the in-plane displacements are satisfied only in weak sense. Next, the computations are repeated by simply subdividing the distorted mesh to validate the element's convergence property in refined mesh, and it is observed that the errors can be effectively eliminated by the mesh refinement.

3.2. The pinched micro cylinder

As shown in Figure 6, the pinched cylinder with end diaphragms is subjected to a pair of opposite concentrated forces in the mid-span. Due to symmetry, only an eighth of the shell is modeled. This is a useful test for evaluating the facet shell element's capability in simulating the inextensional bending and complex membrane deformations. Four different ratios of the material length scale parameter to the shell thickness (l/h=0, 0.1, 0.2, 0.3) are considered. In particular, the case l/h=0 corresponds to the classical elasticity. First, to check the convergence property, the computations are operated using the regular meshes 4×4, 8×8, 16×16 and 24×24. It can be seen from the results summarized in Table 1 that the new element converges rapidly. Besides, Figure 7 gives the distributions of y-direction deflections along the path AB calculated using the regular mesh 24×24, showing that the cylinder shell becomes stiffer as the material length scale parameter increases. Moreover, Figure 8 provides the y-direction deflection contours obtained respectively using the regular mesh and distorted mesh. One can clearly observe that the new element can capture the size effects effectively even though the severely distorted meshes are used.

3.3. The micro hemispherical shells

As shown in Figure 9, this test involves the hemispherical shells subjected to concentrated loads for assessing the influences of geometry warpage on the facet shell element's numerical accuracy. Taking advantage of symmetry, only one quarter of the shell structure is considered. First, the hemispherical shell with an 18° open hole, which is characterized by the inextensional bending deformation and rigid body rotation about the normal to the shell surface, is investigated. The convergences of the z-direction deflections at the load point A for different material length scale parameters are listed in Table 2, while the corresponding deflection contours are given in Figure 10. Second, the full hemispherical shell which experiences more pronounced warping element configurations than the previous one is also analyzed, and the numerical results are provided in Table 3 and Figure 11. It can be easily observed that the proposed facet shell element can still predict the size-dependent mechanical behaviors of small-scale shells very well even when the element' geometry is warped.

3.4. The micro Scordelis-Lo roof

Figure 12 illustrates the well-known Scordelis-Lo roof problem which consists of a cylindrical shell section with end rigid diaphragms and subjected to a self-weight load. Due to symmetry, only a quarter of the roof is analyzed by using both the regular mesh and distorted mesh. The vertical deflections at the load point A calculated using the regular meshes are summarized in Table 4 whilst their distributions along the path AB are provided in Figure 13. Besides, the vertical deflection contours of the roof obtained respectively using the regular and distorted meshes are presented in Figure 14. This test demonstrates once again that the new facet shell element possesses good effectiveness and distortion tolerance in capturing the size effects.

3.5. The micro hyperbolic paraboloid shell

As shown in Figure 15, the hyperbolic paraboloid shell is clamped at one end and subjected to a self-weight load. Owe to symmetry, only a half of the shell is modeled. This is a challenging test for checking the element's performance in modeling the pure bending dominated deformations. The vertical deflections at the point A for different material length scale parameters are summarized in Table 5. Besides, the vertical deflection contours are given in Figure 16. One can clearly observe that the new facet shell element converges rapidly and captures the size dependence of the micro shell efficiently.

4. Conclusion

Within the framework of the modified couple stress elasticity, a quadrilateral 4-node 24-DOF facet shell element is developed for size-dependent static analysis of small-scale thin shell structures with arbitrary geometries. To overcome the interpolation difficulty and mesh distortion sensitivity problems caused by the C^1 continuity requirement, the trial functions that can a priori satisfy related governing differential equations are adopted as the basic functions for element construction whilst the generalized conforming theory and the penalty function method are employed to satisfy the C^1 continuity requirement in weak sense for ensuring the convergence property. Besides, the warpage correction is introduced to take the influence of element's warping geometry into the consideration. To the best of our awareness, there are no other elements of the same type available in the open

literatures. Compared with the IGA elements, the new element has some advantages in versatility and easy applicability. For instance, as the 4-node shell element uses only six conventional DOFs per node, it can be incorporated into the commonly used FE software or programs very directly.

As the present paper mainly focuses on the innovation in the finite element formulation, several classical benchmarks of shells with different geometries are extended to the modified couple stress elasticity for validating the capabilities of the new facet shell element. More realistic engineering problems will be considered in the subsequent works. It is found that the element can simulate the size-dependent mechanical behaviors of small-scale thin shells very effectively. In particular, the facet shell element can still provide satisfactory numerical accuracy even when the element geometry is severely distorted and warped.

Acknowledgements

References

[1] Thai HT, Vo TP, Nguyen TK, Kim SE. A review of continuum mechanics models for size-dependent analysis of beams and plates. Composite Structures 2017; 177: 196-219.

[2] Kong S. A review on the size-dependent models of micro-beam and micro-plate based on the modified couple stress theory. Archives of Computational Methods in Engineering 2021; DOI:10.1007/s11831-021-09567-w.

[3] Zhuang XY, Nguyen BH, Nanthakumar SS, Tran TQ, Alajlan N, Rabczuk T. Computational modeling of flexoelectricity-A review. Energies 2020; 13(6): 1326.

[4] Eringen AC. Linear theory of nonlocal elasticity and dispersion of plane waves. International Journal of Engineering Science 1972; 10(5): 425-435.

[5] Shaat M, Ghavanloo E, Fazelzadeh SA. Review on nonlocal continuum mechanics: Physics, material applicability, and mathematics. Mechanics of Materials 2020; 150: 103587.

[6] Eringen AC, Edelen DGB. On nonlocal elasticity. International Journal of Engineering Science 1972; 10(3): 233-248.

[7] Mindlin RD, Eshel NN. On first strain-gradient theories in linear elasticity. International Journal of Solids and Structures 1968; 4(1): 109-124.

[8] Fleck NA, Muller GM, Ashby MF, Hutchinson JW. Strain gradient plasticity: theory and experiment. Acta Metallurgica et Materialia 1994; 42(2): 475-487.

[9] Altan BS, Aifantis EC. On some aspects in the special theory of gradient elasticity. Journal of the Mechanical Behavior of Materials 1997; 8(3): 231-282.

[10] Hadjesfandiari AR, Dargush GF. Couple stress theory for solids. International Journal of Solids and Structures 2011; 48(18): 2496-2510.

[11] Mindlin RD, Tiersten HF. Effects of couple-stresses in linear elasticity. Archive for Rational Mechanics and Analysis 1962; 11(1): 415-448.

[12] Zozulya V. Higher order couple stress theory of plates and shells. ZAMM-Journal of Applied Mathematics and Mechanics/Zeitschrift für Angewandte Mathematik und Mechanik 2018; 98(10): 1834-1863.

[13] Toupin RA. Elastic materials with couple-stresses. Archive for Rational Mechanics and Analysis 1962; 11(1): 385-414.

[14] Yang F, Chong ACM, Lam DCC, Tong P. Couple stress based strain gradient theory for elasticity. International Journal of Solids and Structures 2002; 39(10): 2731-2743.

[15] Zeighampour H, Beni YT. A shear deformable cylindrical shell model based on couple stress theory. Archive of Applied Mechanics 2015; 85(4): 539-553.

[16] Zeighampour H, Beni YT. Analysis of conical shells in the framework of coupled stresses theory. International Journal of Engineering Science 2014; 81: 107-122.

[17] Jouneghani FZ, Dashtaki PM, Dimitri R, Bacciocchi M, Tornabene F. First-order shear deformation theory for orthotropic doubly-curved shells based on a modified couple stress elasticity. Aerospace Science and Technology 2018; 73: 129-147.

[18] Ghayesh MH, Farokhi H. Nonlinear dynamics of doubly curved shallow microshells. Nonlinear Dynamics 2018; 92(3): 803-814.

[19] Hosseini-Hashemi S, Sharifpour F, Ilkhani MR. On the free vibrations of size-dependent closed micro/nano-spherical shell based on the modified couple stress theory. International Journal of Mechanical Sciences 2016; 115: 501-515.

[20] Ghadiri M, Safarpour H. Free vibration analysis of embedded magneto-electro-thermo-elastic cylindrical nanoshell based on the modified couple stress theory. Applied Physics A 2016; 122(9): 833.

[21] Wang YQ, Liu YF, Zu JW. Size-dependent vibration of circular cylindrical polymeric microshells reinforced with graphene platelets. International Journal of Applied Mechanics 2019; 11(4): 1950036.

[22] Beni YT, Mehralian F, Zeighampour H. The modified couple stress functionally graded cylindrical thin shell formulation. Mechanics of Advanced Materials and Structures 2016; 23(7): 791-801.

[23] Salehipour H, Shahsavar A, Civalek O. Free vibration and static deflection analysis of functionally graded and porous micro/nanoshells with clamped and simply supported edges.

Composite Structures 2019; 221: 110842.

[24] Wang YW, Xie K, Fu TR, Zhang W. A unified modified couple stress model for size-dependent free vibrations of FG cylindrical microshells based on high-order shear deformation theory. European Physical Journal Plus 2020; 135(1): 71.

[25] Garg N, Han CS. A penalty finite element approach for couple stress elasticity. Computational Mechanics 2013; 52(3): 709-720.

[26] Chakravarty S, Hadjesfandiari AR, Dargush GF. A penalty-based finite element framework for couple stress elasticity. Finite Elements in Analysis and Design 2017; 130: 65-79.

[27] Kwon YR, Lee BC. A mixed element based on Lagrange multiplier method for modified couple stress theory. Computational Mechanics 2017; 59(1): 1-12.

[28] Sze KY, Wu ZH. Twenty-four-DOF four-node quadrilateral elements for gradient elasticity. International Journal for Numerical Methods in Engineering 2019; 119(2): 128-149.

[29] Shang Y, Qian ZH, Cen S, Li CF. A simple unsymmetric 4-node 12-DOF membrane element for the modified couple stress theory. International Journal for Numerical Methods in Engineering 2019; 119(9): 807-825.

[30] Deng G, Dargush GF. Mixed Lagrangian formulation for size-dependent couple stress elastodynamic and natural frequency analyses. International Journal for Numerical Methods in Engineering 2017; 109(6): 809-836.

[31] Choi JH, Lee BC. A three-node C^0 triangular element for the modified couple stress theory based on the smoothed finite element method. International Journal for Numerical Methods in Engineering 2018; 114(12): 1245-1261.

[32] Sze KY, Yuan WC, Zhou YX. Four-node tetrahedral elements for gradient-elasticity analysis. International Journal for Numerical Methods in Engineering 2020; 121(16): 3660-3679.

[33] Kwon YR, Lee BC. Three dimensional elements with Lagrange multipliers for the modified couple stress theory. Computational Mechanics 2018; 62(1): 97-110.

[34] Torabi J, Ansari R, Darvizeh M. Application of a non-conforming tetrahedral element in the context of the three-dimensional strain gradient elasticity. Computer Methods in Applied Mechanics and Engineering 2019; 344: 1124-1143.

[35] Shang Y, Li CF, Jia KY. 8-node hexahedral unsymmetric element with rotation DOFs for modified couple stress elasticity. International Journal for Numerical Methods in Engineering 2020; 121(12): 2683-2700.

[36] Papanicolopulos SA, Zervos A, Vardoulakis I. A three dimensional C^1 finite element for gradient elasticity. International Journal for Numerical Methods in Engineering 2009; 77(10): 1396-1415.

[37] Beheshti A. Novel quadrilateral elements based on explicit Hermite polynomials for bending of Kirchhoff-Love plates. Computational Mechanics 2018; 62(5): 1199-1211.

[38] Ansari R, Bazdid-Vahdati M, Shakouri A, Norouzzadeh A, Rouhi H. Micromorphic first-order shear deformable plate element. Meccanica 2016; 51(8): 1797-1809.

[39] Shang Y, Mao YH, Cen S, Li CF. Generalized conforming Trefftz element for size-dependent analysis of thin microplates based on the modified couple stress theory. Engineering Analysis with Boundary Elements 2021; 125: 46-58.

[40] Ansari R, Shojaei MF, Mohammadi V, Bazdid-Vahdati M, Rouhi H. Triangular Mindlin microplate element. Computer Methods in Applied Mechanics and Engineering 2015; 295: 56-76.

[41] Soleimani I, Beni YT, Mehralian F. A new size-dependent cylindrical shell element based on modified couple stress theory. Advances in Applied Mathematics and Mechanics 2018; 10(4): 819-844.

[42] Hughes TJR, Cottrell JA, Bazilevs Y. Isogeometric analysis: CAD, finite elements, NURBS, exact geometry and mesh refinement. Computer Methods in Applied Mechanics and Engineering 2005; 194(39): 4135-4195.

[43] Kolo I, de Borst R. An isogeometric analysis approach to gradient-dependent plasticity. International Journal for Numerical Methods in Engineering 2018; 113(2): 296-310.

[44] Fan F, Safaei B, Sahmani S. Buckling and postbuckling response of nonlocal strain gradient porous functionally graded micro/nano-plates via NURBS-based isogeometric analysis. Thin-Walled Structures 2021; 159: 107231.

[45] Balobanov V, Kiendl J, Khakalo S, Niiranen J. Kirchhoff-Love shells within strain gradient elasticity: Weak and strong formulations and an H-3-conforming isogeometric implementation. Computer Methods in Applied Mechanics and Engineering 2019; 344: 837-857.

[46] Thai TQ, Zhuang XY, Rabczuk T. A nonlinear geometric couple stress based strain gradient Kirchhoff-Love shell formulation for microscale thin-wall structures. International Journal of Mechanical Sciences 2021; 196: 106272.

[47] Schulte J, Dittmann M, Eugster SR, Hesch S, Reinicke T, dell'Isola F, Hesch C. Isogeometric analysis of fiber reinforced composites using Kirchhoff-Love shell elements. Computer Methods in Applied Mechanics and Engineering 2020; 362: 112845.

[48] Wu CJ, Cen S, Ma RX, Li CF. Shape-free arbitrary polygonal hybrid stress/displacement-function flat shell element for linear and geometrically nonlinear analyses. International Journal for Numerical Methods in Engineering 2021; 122(16): 4172-4218.

[49] Long YQ, Xu Y. Generalized conforming triangular membrane element with vertex rigid rotational freedoms. Finite Elements in Analysis and Design 1994; 17(4): 259-271.

[50] Tsiatas GC. A new Kirchhoff plate model based on a modified couple stress theory. International Journal of Solids and Structures 2009; 46(13): 2757-2764.

[51] Long YQ, Cen S, Long ZF. Advanced finite element method in structural engineering. Beijing: Springer & Tsinghua University Press; 2009.

[52] Shang Y, Cen S, Li CF, Fu XR. Two generalized conforming quadrilateral Mindlin-Reissner plate elements based on the displacement function. Finite Elements in Analysis and Design 2015; 99: 24-38.

[53] Allman DJ. A compatible triangular element including vertex rotations for plane elasticity analysis. Computers & Structures 1984; 19(1-2): 1-8.

[54] Zienkiewicz OC, Xu ZN, Zeng LF, Samuelsson A, Wiberg NE. Linked interpolation for Ressiner-Mindlin plate element: part I- a simple quadrilateral. International Journal for Numerical Methods in Engineering 1993; 36(18): 3043-3056.

[55] Cen S, Fu XR, Zhou MJ. 8-and 12-node plane hybrid stress-function elements immune to severely distorted mesh containing elements with concave shapes. Computer Methods in Applied Mechanics and Engineering 2011; 200(29): 2321-2336.

[56] Boutagouga D. A review on membrane finite elements with drilling degree of freedom. Archives of Computational Methods in Engineering 2021; 28(4): 3049-3065.

[57] Ibrahimbegovic A, Taylor RL, Wilson EL. A robust quadrilateral membrane finite element with drilling degrees of freedom. International Journal for Numerical Methods in Engineering 1990; 30(3): 445-457.

[58] Ibrahimbegovic A. A novel membrane finite element with an enhanced displacement interpolation. Finite Elements in Analysis and Design 1990; 7(2): 167-179.

[59] Iura M, Atluri S. Formulation of a membrane finite element with drilling degrees of freedom. Computational Mechanics 1992; 9(6): 417-428.

[60] Taylor RL. Finite element analysis of linear shell problems. Whiteman, JR (ed), Proceedings of the Mathematics in Finite Elements and Applications1987. p. 191-203.

[61] ABAQUS. ABAQUS 2016 documentation Dassault systems. Providence2016.

[62] Soh AK, Chen WJ. Finite element formulations of strain gradient theory for microstructures and the C^{0-1} patch test. International Journal for Numerical Methods in Engineering 2004; 61(3): 433-454.

[63] Belytschko T, Leviathan I. Physical stabilization of the 4-node shell element with one point quadrature. Computer Methods in Applied Mechanics and Engineering 1994; 113(3): 321-350.

[64] Macneal RH, Harder RL. A proposed standard set of problems to test finite element accuracy. Finite elements in Analysis and Design 1985; 1(1): 3-20.

[65] Parisch H. An investigation of a finite rotation four node assumed strain shell element. International Journal for Numerical Methods in Engineering 1991; 31(1): 127-150.

[66] Shang Y, Cen S, Li CF. A 4-node quadrilateral flat shell element formulated by the shape-free HDF plate and HSF membrane elements. Engineering Computations 2016; 33(3): 646-666.

[67] Bathe KJ, Iosilevich A, Chapelle D. An evaluation of the MITC shell elements. Computers & Structures 2000; 75(1): 1-30.

Table 1. The y-direction deflections at the load point A of the pinched cylinder (μm)

Mesh	4×4	8×8	16×16	24×24	Reference
l/t=0	11.2815	16.4817	17.8972	18.1129	18.248 [63]
l/t=0.1	11.0778	16.1006	17.4535	17.6596	17.866[*]
l/t=0.2	10.5288	15.0877	16.2804	16.4625	16.636[*]
l/t=0.3	9.7746	13.7305	14.7233	14.8757	15.017[*]

[*]The reference values are obtained using 200000 hexahedral solid element [35]

Table 2. The *z*- deflections at the point A of the hemispherical shell with 18° open hole (μm)

Mesh	4×2×2	4×4×4	4×8×8	Reference
l/t=0	3.91213	8.96532	9.32594	9.4 [64]
l/t=0.1	3.73365	8.05685	8.35010	8.3733[*]
l/t=0.2	3.28506	6.18770	6.36634	6.3857[*]
l/t=0.3	2.73890	4.47548	4.57618	4.5915[*]

[*]The reference values are obtained using 100000 hexahedral solid element [35]

Table 3. The z- deflections at the point A of the full hemispherical shell (μm)

Mesh	3×2×2	3×4×4	3×8×8	Reference
l/t=0	3.57011	8.74082	9.20547	9.24 [65]
l/t=0.1	3.42115	7.86503	8.24175	8.2756[*]
l/t=0.2	3.04094	6.05476	6.28238	6.3075[*]
l/t=0.3	2.56652	4.38704	4.51416	4.5332[*]

[*]The reference values are obtained using 75930 hexahedral solid element [35]

Table 4. The vertical deflections at the point A of the micro roof (μm)

Mesh	4×4	8×8	16×16	Reference
l/t=0	3.13487	3.03047	3.01112	3.024 [66]
l/t=0.1	2.94726	2.85236	2.83466	2.8375[*]
l/t=0.2	2.50993	2.43589	2.42185	2.4243[*]
l/t=0.3	2.03244	1.97899	1.96867	1.9713[*]

[*]The reference values are obtained using 200000 hexahedral solid element [35]

Table 5. The vertical deflections at the point A of the hyperbolic paraboloid shell (μm)

Mesh	8×4	16×8	32×16	64×32	Reference
l/t=0	3.53532	6.09765	6.30851	6.35857	6.394 [67]
l/t=0.1	3.48078	5.92452	6.12791	6.17466	6.2577[*]
l/t=0.2	3.35309	5.49360	5.66379	5.70349	5.8383[*]
l/t=0.3	3.16550	4.93497	5.06837	5.10097	5.1213[*]

[*]The reference values are obtained using 200000 hexahedral solid element [35]
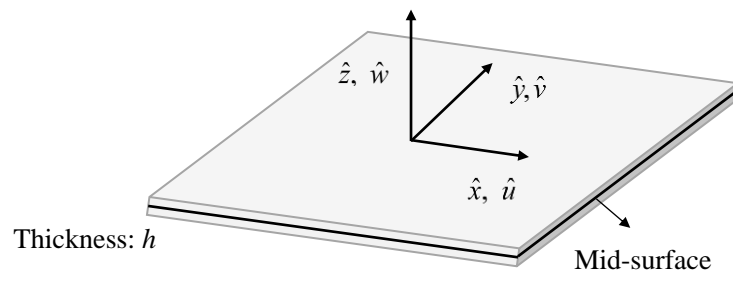
Figure 1. The schematic representation of a thin flat subdomain
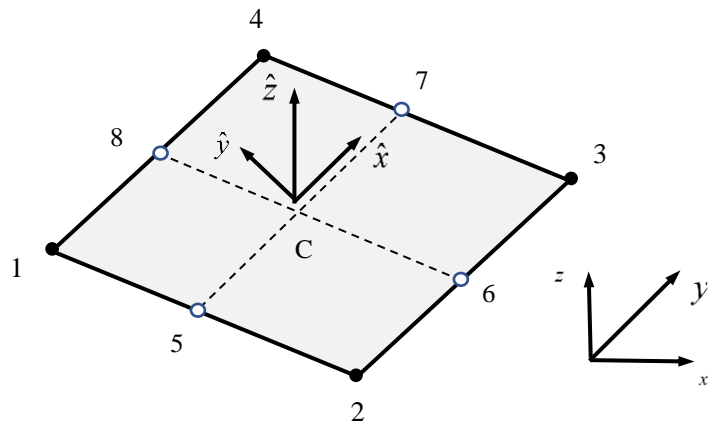
Figure 2. The quadrilateral 4-node facet shell element
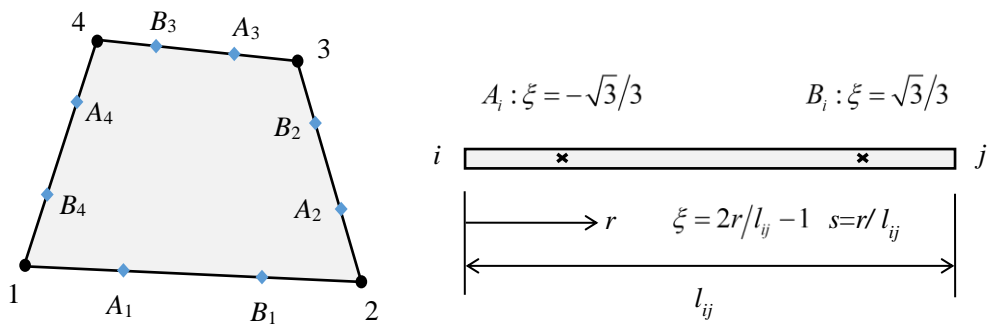
Figure 3. The points of the edge *ij* for imposing compatibility conditions
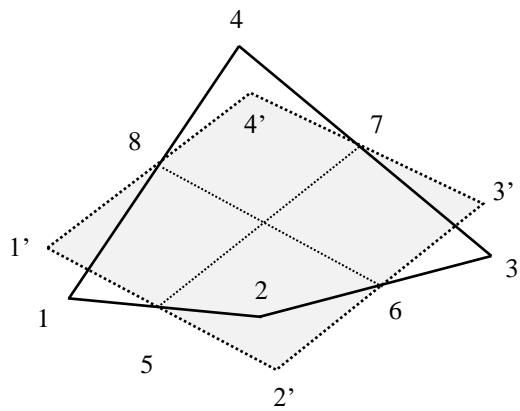
Figure 4. The projection of warped element into flat one

Mesh A   Mesh B   Mesh C
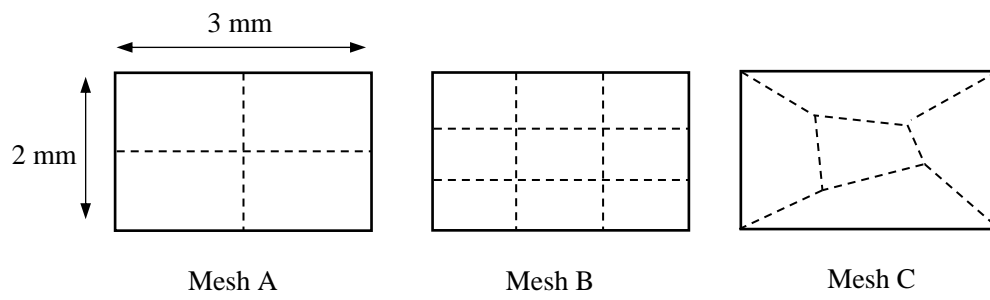
E=4×10^{5}MPa, ν=0.3, t=10μm, l=10μm

Figure 5. The meshes for the patch test
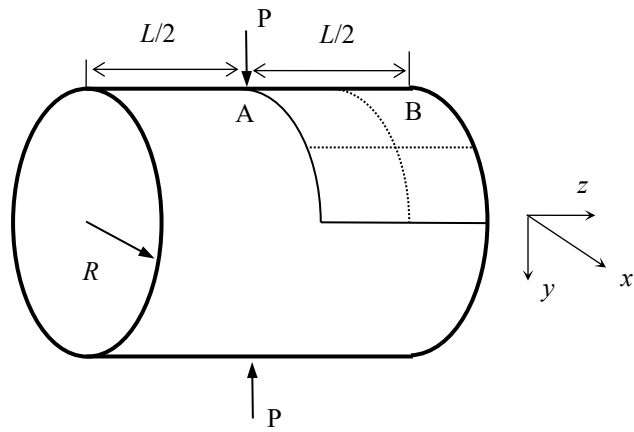
R=3mm, L=6mm, t=30μm, E=3×10^{5}Mpa, v=0.3, P=1N

Figure 6. The pinched micro cylinder
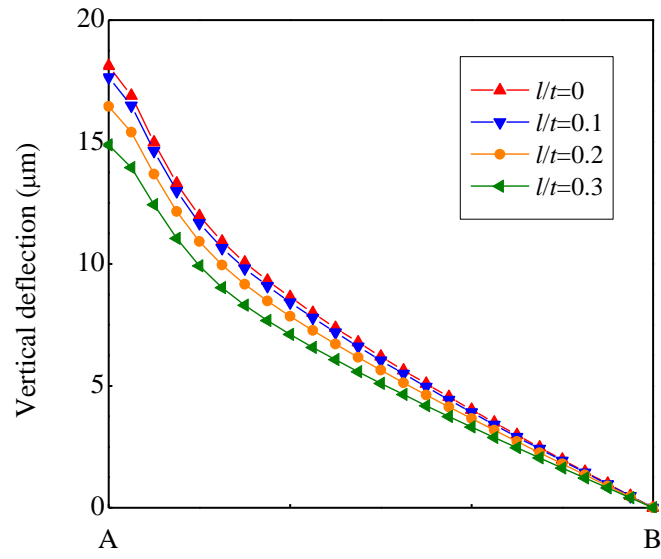
Figure 7. The distributions of *y*-direction deflections along the path AB of
the pinched cylinder obtained using the regular mesh 24×24
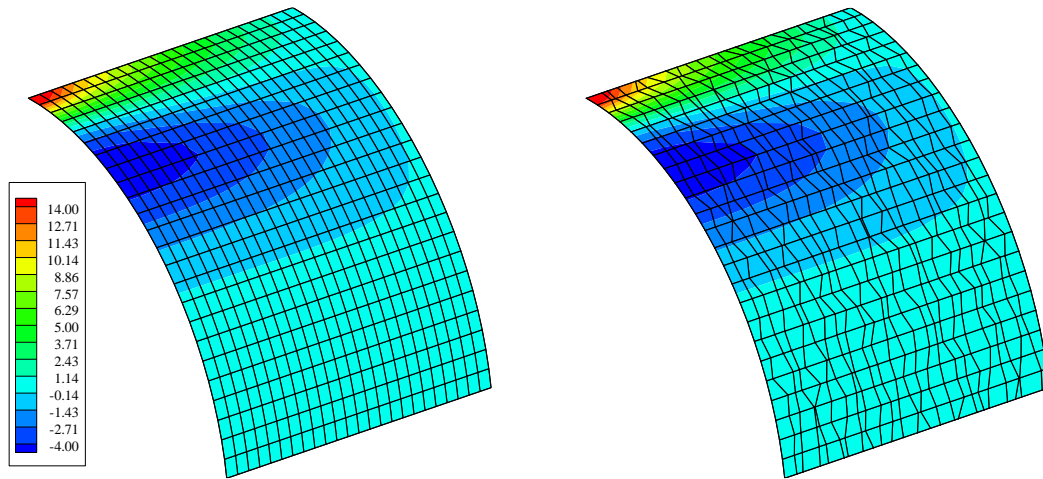
(a) *l/t*=0.1
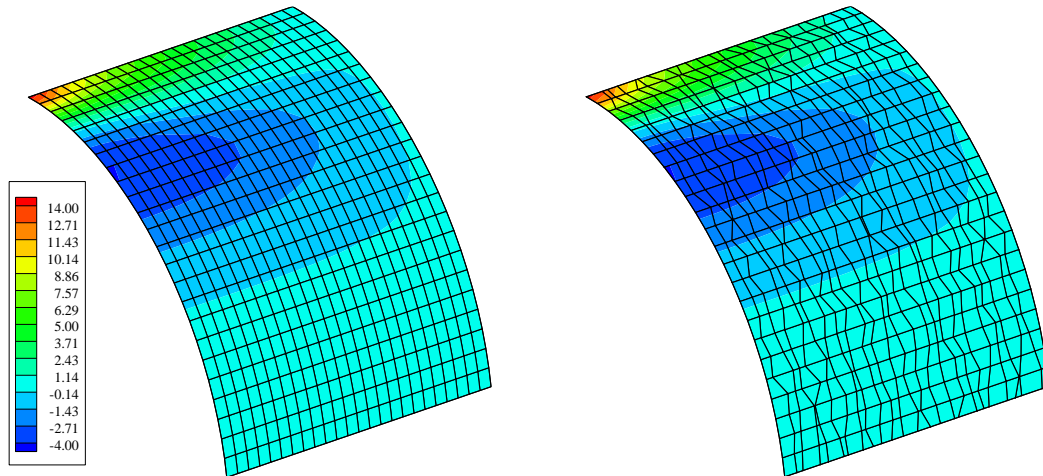
(b) *l/t*=0.3

Figure 8. The *y*-direction deflection contours of the pinched cylinder obtained
respectively using the regular and distorted meshes (μm)
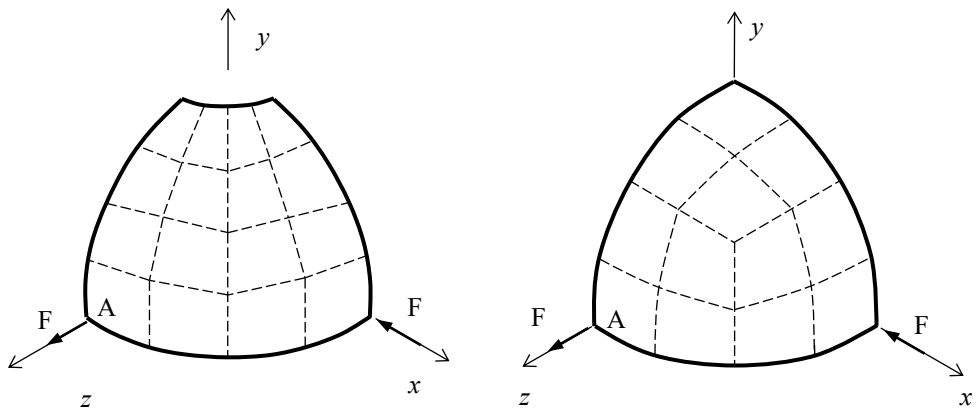
R=10mm, t=40μm, E=6.825×10^{5}Mpa, v=0.3, F=1×10^{-3}N

Figure 9. (a) Hemispherical shell with 18° hole; (b) Full hemispherical shell.

(a) *l/t*=0

(b) *l/t*=0.1

(c) *l/t*=0.2

(d) *l/t*=0.3
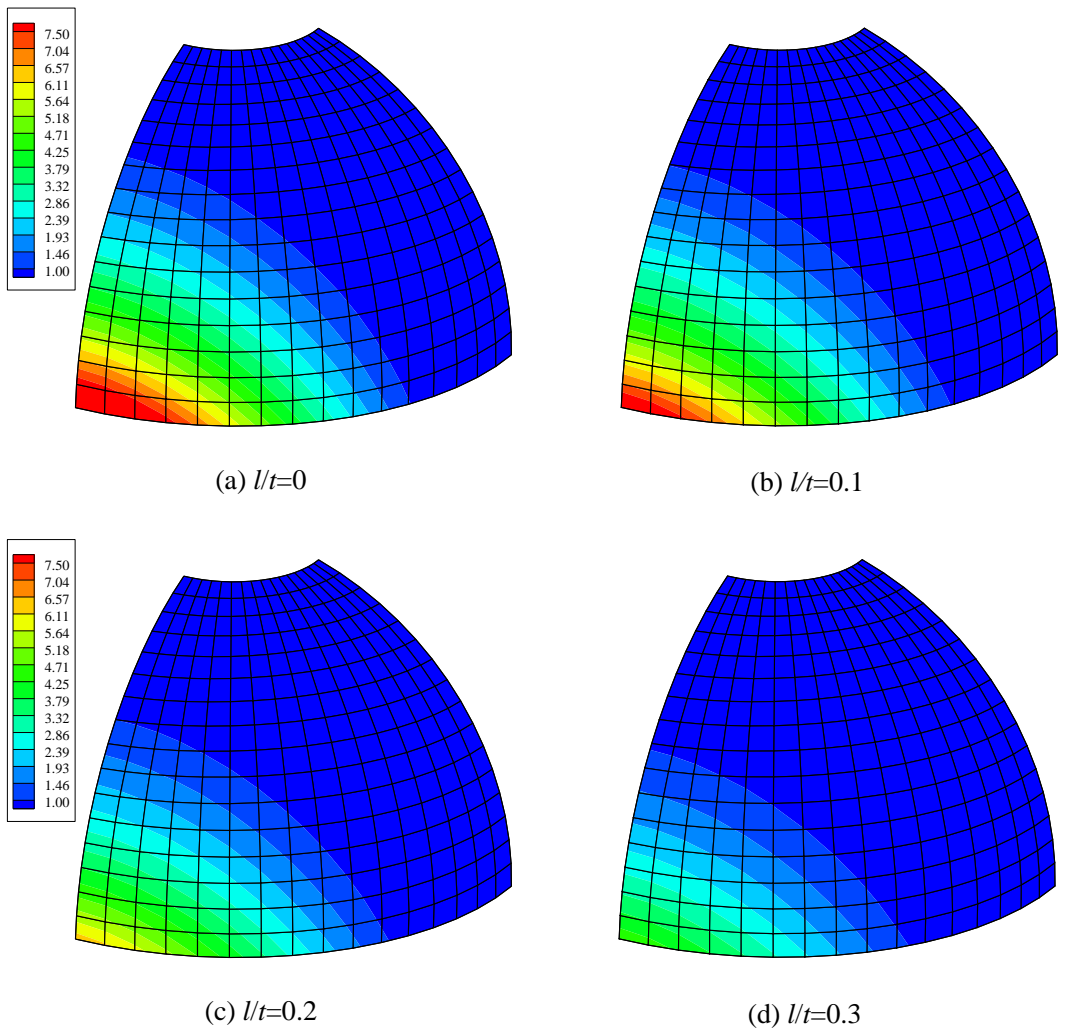
Figure 10. The *z*- deflection contours of the hemispherical shell with 18° open hole (μm)

(a) *l*/*t*=0

(b) *l*/*t*=0.1

(c) *l*/*t*=0.2

(d) *l*/*t*=0.3
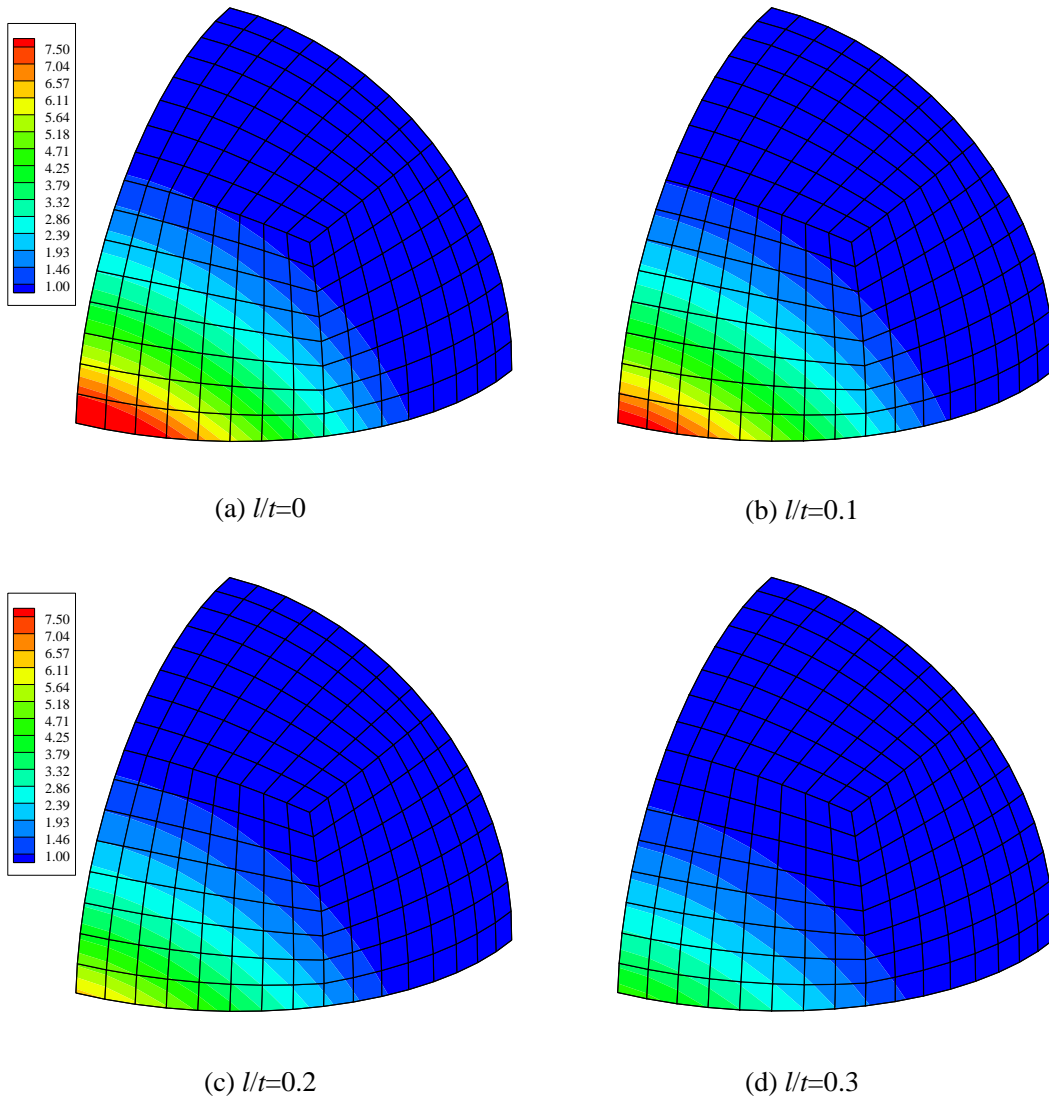
Figure 11. The *z*- deflection contours of the full hemispherical shell (μm)
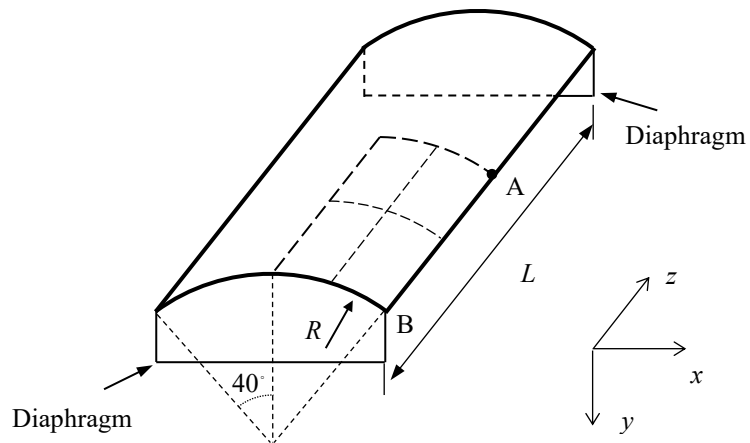
R=2.5mm, L=5mm, t=25μm, E=4.32×10^{5}MPa, ν=0, self-weight 9×10^{-3}N/mm^2

Figure 12. The micro roof
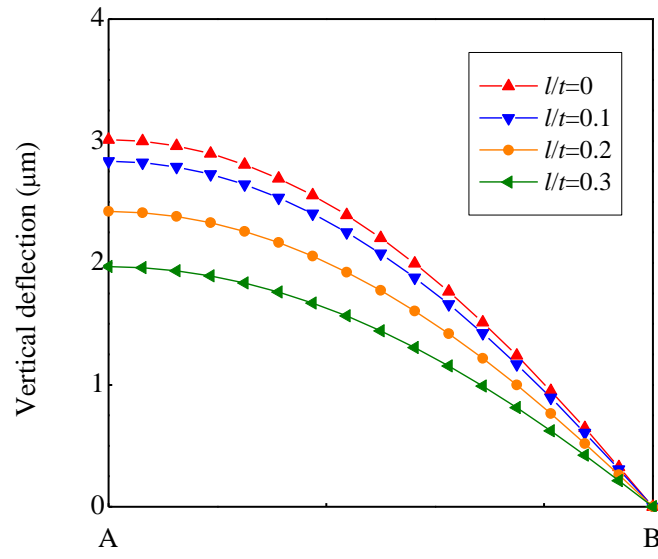
Figure 13. The distributions of the vertical deflections along the path AB
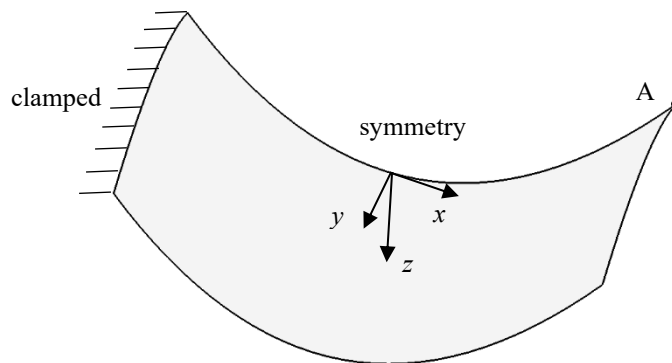of the micro roof using the regular mesh 16×16
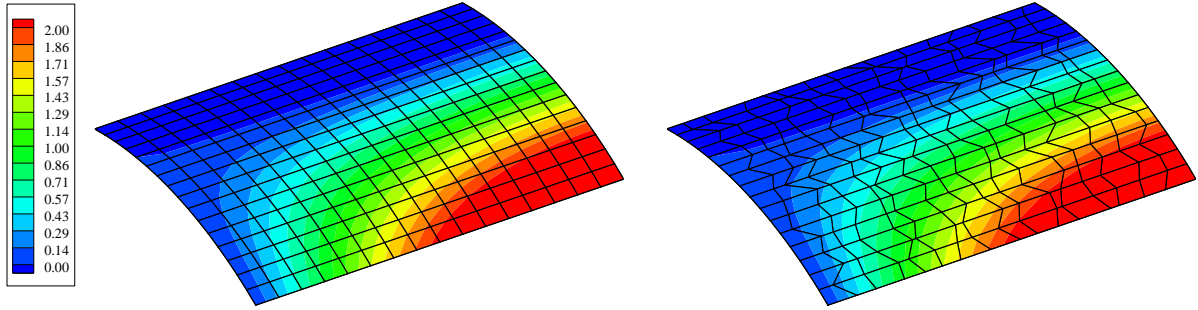
(a) *l*/*t*=0.1
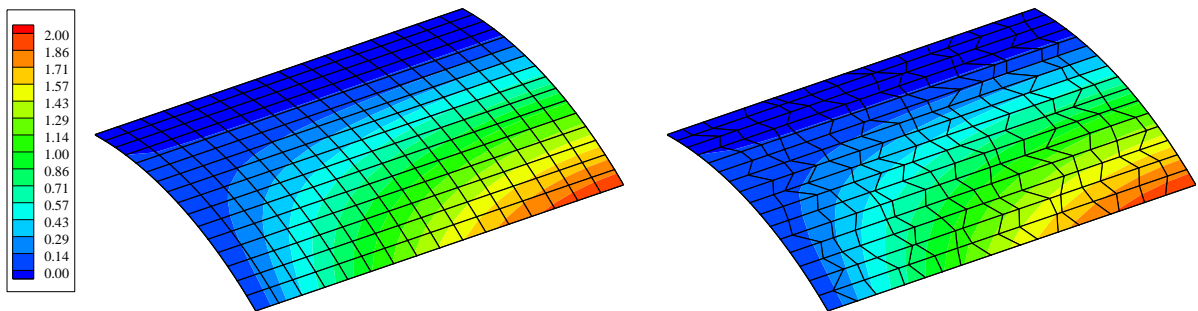
(b) *l*/*t*=0.3

Figure 14. The vertical deflection contours of the roof obtained respectively using the regular and distorted meshes (μm)

$t=1\mu\mathrm{m}$, $E=2\times10^7\mathrm{MPa}$, $\nu=0.3$, self-weight $8.0\times10^{-4}\mathrm{N/mm^2}$

$z=x^2-y^2$, x [−0.5, 0.5], y [−0.5, 0] (mm)

Figure 15. Partly clamped hyperbolic paraboloid shell

(a) *l*/*t*=0

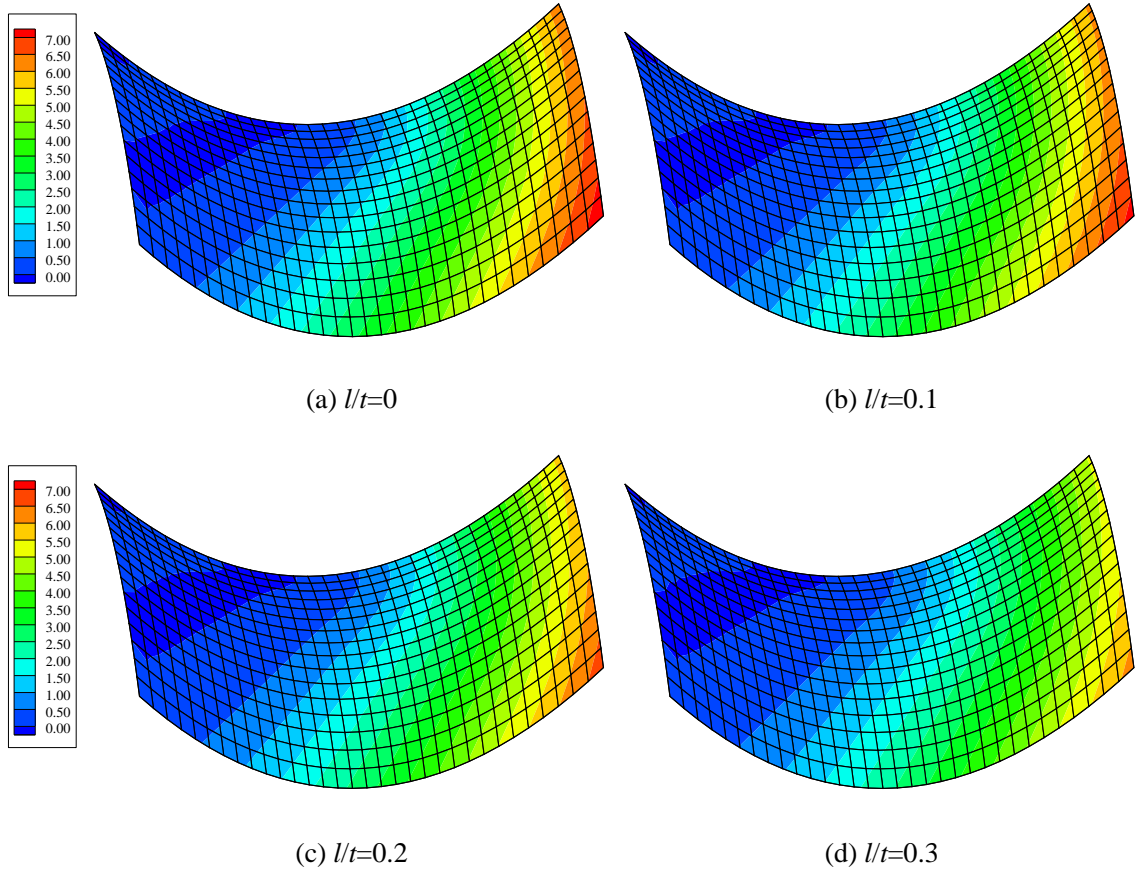(b) *l*/*t*=0.1

(c) *l*/*t*=0.2

(d) *l*/*t*=0.3

Figure 16. The *z*- deflection contours of the hyperbolic paraboloid shell (μm)